Desalination and Water Treatment
www.deswater.com

doi: 10.5004/dwt.2019.24227

161 (2019) 76–91
September

A flux boundary scheme in the lattice Boltzmann method and its applications in the simulation of membrane desalination

Wende Li[a,*], Xu Su[a], Alan Palazzolo[a], Shehab Ahmed[b]

[a]*Department of Mechanical Engineering, Texas A&M University, College Station, TX 77840, United States, emails: wende.li@outlook.com (W. Li), sxdl92victor@tamu.edu (X. Su), a-palazzolo@tamu.edu (A. Palazzolo)*
[b]*Department of Electrical Engineering, Texas A&M University at Qatar, Doha, Qatar, email: sahmed18@gmail.com*

Received 6 August 2018; Accepted 3 April 2019

ABSTRACT

In membrane desalination processes, such as brackish water and seawater desalination, the concentration polarization (CP) and surface fouling are remarkable features affecting the performance of these filtration technologies. In this paper, a flux boundary scheme in the lattice Boltzmann method is proposed to predict the CP and inorganic fouling growth on the membrane surface. The proposed flux boundary scheme can be used to prescribe mass flux directly on the boundary, without the normal derivative calculation nor the boundary neighboring nodes interpolation. The flux boundary scheme is numerically validated with a number of cases including different flux boundary conditions. Successful applications of the proposed flux boundary scheme to large Peclet number convection–diffusion desalination processes reveal the CP and fouling phenomena. Results of the CP and permeate flux prediction are compared with a finite element method (FEM) benchmark in a complete rejection condition. Simulation results show that the CP is reduced with a rejection rate considered, that is, without the complete rejection assumption. A higher membrane rejection rate results in better product water quality, but this is accompanied by a higher CP and lower permeate flux. This conclusion indicates a trade-off between membrane selectivity (salt rejection) and membrane permeability (permeate flux). When applied to the simulation of inorganic fouling growth in membrane desalination, the present flux boundary scheme provides results that agree well with reported results in terms of the crystal size, mass accumulation and concentration distribution. The proposed flux boundary scheme has a first-order accuracy for both straight boundaries and curved boundaries.

Keywords: Flux boundary scheme; Mass transport; Membrane filtration; Lattice Boltzmann method; Concentration polarization; Inorganic fouling

1. Introduction

Pressure-driven membrane filtration technologies for seawater desalination and wastewater treatment consume less energy than thermal distillation technologies [1]. However, membrane filtration is still limited by several aspects. For example, membrane filtration usually is feedwater quality sensitive, has relatively low production rate and suffers membrane fouling. Also, the inherent concentration polarization (CP) reduces the transmembrane pressure and plays a vital role in triggering surface fouling. The CP arises when a portion of water solvent passes through the membrane and rejected solute ions tend to accumulate in the vicinity of the membrane surface. A steady-state concentration gradient will be established when the solute convection process is balanced by the solute back-diffusion process. Thus, the CP leads to an elevated solute concentration near the membrane surface. Although a variety of methods have been developed to predict the CP phenomenon, such as the classical stagnant film model [2], traditional numerical methods (finite difference method and finite element method) [3] and computational fluid dynamics methods [4,5], a complete membrane salt rejection (a 100% rejection rate) was usually assumed. For example, the reverse osmosis (RO) membrane has a

* Corresponding author.

rejection rate up to 99.8%, and at least 96.875% is required to achieve the drinking standard (1,000 mg/L) for the permeate product in seawater desalination (the source water concentration assumed to be 32,000 mg/L). The membrane rejection rate directly affects the accumulation of salt ions near the membrane surface, thus the CP should vary with different salt rejection rates. So, it is of significance to incorporate the membrane rejection rate into the CP prediction model. Without the complete rejection assumption and with the membrane rejection rate considered, a portion of salt ions can be transported through the membrane to the permeate water side, and in this situation, the transport mass flux boundary should be adopted to describe the filtration process with the rejection rate considered.

Increased concentration near the membrane surface may cause over-saturation of sparingly soluble salts including calcium sulfate dihydrate (gypsum), calcium carbonate (calcite) and barium sulfate (barite), especially in the desalination process of brackish water with higher recovery. When the mineral salt concentration exceeds the salts saturation, mineral scaling on the membrane surface (due to homogenous and heterogeneous mineral salt crystallization) decreases the available surface for water permeation, leading to a decline in overall flux and shortening of the membrane lifetime [4]. The main fouling mechanism is crystallization on the membrane surface [6] by inorganic salts such as the aforementioned $CaSO_4$, $CaCO_3$ and $BaSO_4$. During the pressure-driven membrane filtration process, ions from these most common inorganic salts are rejected and a CP layer will be formed, which results in an initial flux decline due to the increase of the osmotic pressure (or the transmembrane pressure). If nucleation of inorganic salts occurs in an over-saturation condition, a scaling layer will form on the membrane surface and induce a further flux decline. Inorganic fouling growth is often a slow kinetic process, and fouling mitigation strategies typically rely on thermodynamic solubility calculations and experimental trial and error. Numerical modeling could be an effective and economical method for the direct simulation of fouling growth and the characterization of the local flow and concentration fields.

The lattice Boltzmann method (LBM) has been developed as a viable and effective computational method for fluid dynamics simulation and chemical processes modeling. Different from conventional numerical methods, which are based on the discretization of macroscopic continuum equations, LBM stems from the kinetic theory and describes a system from the macroscopic scale [7]. Beyond successful applications in complex fluid dynamics [8–10], LBM possesses wide applications in energy and environmental science (such as the heat and mass transfer in heterogeneous media [11]), chemical engineering (such as the chemical dissolution in porous media [12]), geology (such as the transport in saturated karst [13]) and so on. Recently, LBM has been applied to the prediction of microfiltration and water treatment processes. Kromkamp et al. [14] developed an LBM model to simulate the hydrodynamics of a suspension flow and the CP in cross-flow microfiltration. Torkkeli [15] reported numerical predictions of biofilm growth in porous media using LBM, which showed a promising applicability of this numerical method in the simulation of the coupled fluid dynamics and mass transport processes. Although boundary schemes for fluid dynamics have well been established, they are still largely based on a non-local finite difference treatment for mass transport processes. The implementation of the Dirichlet boundary condition in LBM is well known, however, the Neumann boundary condition is still tricky since the calculation of the normal derivative (the gradient normal to the boundary) in LBM cannot be directly accessed and implemented. One treatment in LBM is to convert the Neumann boundary to the Dirichlet boundary using the finite difference approximation for the normal derivative [16].

In this paper, a novel mass flux boundary scheme is proposed in LBM without using the finite difference approximation or the interpolation treatment shown in existing boundary schemes. The proposed boundary scheme is tested and compared with benchmark cases. A membrane desalination CP prediction model incorporating the salt rejection rate using the proposed mass flux boundary scheme is developed. Thereafter, the developed boundary scheme is applied to study inorganic fouling growth on the membrane surface. Standard single-relaxation-time LBM is used in benchmark cases and application models.

1.1. Background

The convection–diffusion equation for a physical quantity without sources or sinks can be shown in Eq. (1).

$$\frac{\partial C}{\partial t} + \nabla \cdot \left(\mathbf{u}C - D\nabla C \right) = 0 \tag{1}$$

In Eq. (1) C is the variable of interest (such as the species concentration for mass transfer, or temperature for heat transfer), D is the diffusivity or diffusion coefficient (such as mass diffusivity for particle motion, or thermal diffusivity for heat transport), and $\mathbf{u}$ is the given velocity that the quantity is moving with. A general mathematical definition of total flux $\mathbf{J}_\sigma$ due to convection and diffusion can be given by Eq. (2). In this paper, flux is by default heat flux in heat transfer or mass flux in mass transport, instead of flow mass flux $\rho\mathbf{u}$ in fluid dynamics.

$$\mathbf{J}_\sigma = \mathbf{u}C - D\nabla C \tag{2}$$

Flux normal to the boundary ($\mathbf{J}_\sigma \cdot \mathbf{n}$) is critical in the numerical simulation of processes including heat transfer in fluid, mass transport in porous media, chemical reactions, and the membrane filtration, and so on. To prescribe the heat or mass flux on the boundary, traditional finite-difference schemes are generally required to compute the temperature gradient or the concentration gradient. For LBM, the unknown post-streaming distribution functions on the boundary can also be calculated by the interpolation of the post-collision distribution functions on the boundary-neighboring nodes to continue to numerical calculation [17]. In finite difference type boundary schemes and nodes interpolation type boundary schemes, boundary-neighboring nodes besides boundary local nodes will be involved to calculate the unknown post-streaming distribution functions on the boundary. However in this study, the proposed flux boundary scheme involves the distribution functions at local

boundary nodes only without using boundary-neighboring nodes, and such local on-site nodes boundary schemes are desirable to deal with problems with complex geometries, such as mass transport in porous media [17]. As a result, an on-site flux boundary scheme in LBM without the finite difference approximation or the interpolation treatment should be useful for the simulation of convection–diffusion processes with complex geometries involved.

1.2. Existing flux boundary schemes in LBM

The flux boundary $\partial\Omega$ can be described by a Robin boundary (or called third type boundary), which is a weighted combination of the Neumann boundary and the Dirichlet boundary, as seen in Eq. (3).

$$\alpha_1 \frac{\partial C}{\partial \mathbf{n}} + \alpha_2 C = \alpha_3, \quad 0 < t < t_s, \mathbf{x} \in \partial\Omega \tag{3}$$

In Eq. (3), **n** is the unit normal vector pointing outward of the boundary $\partial\Omega$ from the solid phase to the fluid phase, coefficients α_k (k = 1, 2, 3) should be given functions of space **x** and time t, and t_s is a pre-specified simulation time. Specifically, if $\alpha_1 = 0$ and $\alpha_2 \neq 0$, Eq. (3) represents a Dirichlet boundary condition; if $\alpha_1 \neq 0$ and $\alpha_2 = 0$, Eq. (3) represents a Neumann boundary condition.

In LBM, the Neumann boundary can be transformed into the Dirichlet boundary by the finite difference method to approximate the normal derivative [16,18]. Another treatment in LBM is to calculate the unknown post-streaming distribution functions on the boundary by interpolating the neighboring boundary nodes [17,19]. Taking the first treatment as an example, the normal derivative of the concentration in a mass transport process can be approximated by the unknown wall concentration C_w at the wall node $\mathbf{x}_w$ and the known concentration C_f at the neighboring fluid node $\mathbf{x}_f$ along the normal direction, as shown in Eq. (4).

$$D\frac{\partial C}{\partial n} \approx D\frac{C_f - C_w}{\left|x_f - x_w\right|} \tag{4}$$

Note that in the right-hand side of Eq. (4), the numerator of the finite difference approximation should always be $(C_f - C_w)$ considering the direction of the unit normal vector **n**. Then the calculated wall concentration C_w will be imposed to calculate the unknown post-streaming distribution functions following exactly the Dirichlet boundary treatment by an anti-bounce-back scheme, as shown in Eq. (5) [16,18,20].

$$g_{i^*}\left(\mathbf{x}_{fi}, t+\delta t\right) = -g^{+}\left(\mathbf{x}_{fi}, t\right) + 2w\,C_w \tag{5}$$

In Eq. (5), g_i^+ is known as the post-collision distribution function at node $\mathbf{x}_f$, g_{i^*} is the unknown post-streaming distribution function in the opposite direction of g_i^+, and w_i is the weight coefficient for i = 0 ~ 8. For interpolation type boundary schemes, unknown post-streaming distribution functions can be calculated by interpolating known post-collision distribution functions at boundary-neighboring nodes with a series of carefully chosen interpolation coefficients [17–19]. However, interpolation-based schemes for treatment of curved boundaries destroy mass conservation near the boundary and the interpolation-free approaches in LBM for curved boundaries can improve the accuracy of the computed results [21].

Yoshino and Inamuro [22] proposed a flux boundary scheme in LBM which can be used to impose the flux boundary directly without using the finite difference nor the interpolation treatment. However, this boundary scheme was based on an assumption that mass flux of σ-species normal through the boundary is zero, and the unknown wall concentration at the boundary C_w is specified by Eq. (6).

$$C_w = -\frac{\sum_{i(\mathbf{c}_i\cdot\mathbf{n}\le 0)} g_i \mathbf{e}_i \cdot \mathbf{n}}{\sum_{i(\mathbf{c}_i\cdot\mathbf{n}>0)} w_i \mathbf{e}_i \cdot \mathbf{n}} \tag{6}$$

The calculated wall concentration C_w will be used to calculate the unknown distribution functions by $g_i = w_i C_w$ ($\mathbf{e}_i \cdot \mathbf{n} > 0$). Since this flux boundary scheme assumes that normal flux through the boundary is zero, it could be called a zero-flux boundary scheme. This zero-flux boundary scheme can be used to predict the membrane CP under a complete rejection assumption (a 100% rejection rate).

2. Development of the present flux boundary scheme

2.1. Lattice Boltzmann model

Mass transport of salts ions in feed water during membrane filtration can be described by the convection–diffusion process. The feed water is assumed to be incompressible in this study due to the low cross-flow velocity (about 0.1 m/s) in the feed channel. Two sets of particle distribution functions are employed to simulate the convection–diffusion process. One set of distribution function is adopted to solve fluid dynamics and another set of distribution function is adopted to solve mass transport. The evolution of distribution functions is governed by the lattice Boltzmann equations [16–18] as shown in Eq. (7).

$$\begin{cases} f_i\left(\mathbf{x}+\mathbf{e}_i\delta t, t+\delta t\right) - f_i\left(\mathbf{x},t\right) = -\dfrac{1}{\tau}\left[f_i\left(\mathbf{x},t\right) - f_i^{eq}\left(\mathbf{x},t\right)\right] \\ g_i\left(\mathbf{x}+\mathbf{e}_i\delta t, t+\delta t\right) - g_i\left(\mathbf{x},t\right) = -\dfrac{1}{\tau_s}\left[g_i\left(\mathbf{x},t\right) - g_i^{eq}\left(\mathbf{x},t\right)\right] \end{cases} \tag{7}$$

In Eq. (7), $f_i(\mathbf{x},t)$ and $g_i(\mathbf{x},t)$ are the distribution functions for the fluid field and the concentration field, respectively, at space **x** and time t, and f_i^{eq} and g_i^{eq} are the equilibrium distribution functions for f_i and g_i, respectively. The subscript of the distribution functions i is used to distinguish lattice speed directions, $\mathbf{e}_i$ denotes the lattice velocities, δt is the time increment, τ and τ_s are the non-dimensional relaxation times for f_i and g_i, respectively. The kinematic viscosity ν and the diffusivity (diffusion coefficient) D are related to the dimensionless relaxation times by Eq. (8).

$$\begin{cases} \nu = \dfrac{\left(\tau - 1/2\right)c^2\delta t}{3} \\ D = \dfrac{\left(\tau_s - 1/2\right)c^2\delta t}{3} \end{cases} \tag{8}$$

The equilibrium distribution functions must be defined appropriately so that the mass and momentum are conserved [23]. For small fluid velocities and small Mach numbers, the equilibrium distribution functions in Eq. (7) can be defined as Eq. (9) [22] in order to recover the Navier–Stokes equations and the convection–diffusion equation.

$$\begin{cases} f_i^{eq}=w_i\rho\left[1+\dfrac{\mathbf{e}_i\cdot\mathbf{u}}{c_s^2}+\dfrac{\left(\mathbf{e}_i\cdot\mathbf{u}\right)^2}{2c_s^4}-\dfrac{\mathbf{u}\cdot\mathbf{u}}{2c_s^2}\right] \\ g_i^{eq}=w_iC\left[1+\dfrac{\mathbf{e}_i\cdot\mathbf{u}}{c_s^2}\right] \end{cases} \tag{9}$$

In Eq. (9), $\mathbf{u}$ is the fluid velocity, ρ is the fluid density, C is the solute mass concentration, and w_i is the weight coefficient. Also, the lattice sound speed $c_s = c/\sqrt{3}$, and in which the lattice speed $c = \delta h/\delta t = 1$ for a standard square lattice, and the lattice spacing $\delta h = \delta x = \delta y$ and the lattice time step $\delta t = 1$. Weight coefficients $w_0 = 4/9$, $w_i = 1/9$ for $i = 1$~4, and $w_i = 1/36$ for $i = 5$~8 for a D2Q9 lattice model. The discrete velocity $\mathbf{e}_i$ is given by Eq. (10) as follows:

$$\mathbf{e}_i=\begin{cases} (0,0) & i=0 \\ c\left\{\cos\left[\dfrac{(i-1)\pi}{2}\right],\sin\left[\dfrac{(i-1)\pi}{2}\right]\right\} & i=1,2,3,4 \\ \sqrt{2}c\left\{\cos\left[\dfrac{(2i-9)\pi}{4}\right],\sin\left[\dfrac{(2i-9)\pi}{4}\right]\right\} & i=5,6,7,8 \end{cases} \tag{10}$$

The macroscopic properties, including the fluid density ρ, the fluid velocity $\mathbf{u}$, the fluid pressure P, and the concentration C, are readily available from the distribution functions as shown in Eq. (11).

$$\rho=\sum_{i=0}^{8}f_i,\ \mathbf{u}=\frac{1}{\rho}\sum_{i=0}^{8}\mathbf{e}_i f_i,\ P=c_s^2\rho,\ C=\sum_{i=0}^{8}g_i \tag{11}$$

Both the Navier–Stokes equations and the convection–diffusion equation can be recovered from the equilibrium distribution functions shown in Eq. (9) via the Chapman–Enskog analysis with a second-order accuracy [24,25]. In LBM, the domain and the boundary are discretized and the distribution functions are solved locally at each node by the collision process and the streaming process, and then the macroscopic parameters are determined following Eq. (11).

2.2. Present flux boundary scheme

Flux is an important physical variable in heat transfer and mass transport involving both convection and diffusion. Chai and Zhao [26] proposed a numerical method to calculate boundary mass flux in the LBM framework, however, this method was not extended as a boundary scheme to prescribe boundary flux. Physically, heat and mass flux can be calculated directly through the flux definition shown in Eq. (2), and the gradient of the variable on boundary nodes or in interior lattice nodes can be computed by Eq. (12) [17,27].

$$\nabla C=\frac{3}{\tau}\frac{\delta t}{\delta h^2}\left(\mathbf{u}C-\sum_{i=0}^{8}g_i\mathbf{e}_i\right) \tag{12}$$

In this study, Eq. (12) is slightly different than the form in the study proposed by Huang and Yong [17] since the lattice speed is included in the discrete velocities $\mathbf{e}_i$ as shown in Eq. (10). After a rearrangement of Eqs. (12) and (13) can be obtained.

$$\left(\sum_{i=0}^{8}g_i\mathbf{e}_i\right)\cdot\mathbf{n}=\left(\mathbf{u}C-\frac{\tau}{3}\frac{\delta h^2}{\delta t}\nabla C\right)\cdot\mathbf{n} \tag{13}$$

The present flux boundary scheme is based on a finding that total flux normal through the boundary equals the projection of the first-order moment of distribution functions on the surface normal, and in which, the known distribution functions should be in a post-collision form while the unknown distribution functions should be in a post-streaming form, as shown in Eq. (14).

$$\underbrace{\sum_{\mathbf{e}_i\cdot\mathbf{n}>0}g_i\mathbf{e}_i\cdot\mathbf{n}}_{\text{unkonwn}}+\underbrace{\sum_{\mathbf{e}_i\cdot\mathbf{n}\le 0}g_i^{+}\mathbf{e}_i\cdot\mathbf{n}}_{\text{konwn}}=\left(\mathbf{u}C-D\nabla C\right)\cdot\mathbf{n}=\mathbf{J}_\sigma\cdot\mathbf{n} \tag{14}$$

The detailed derivation of Eq. (14) can be seen in Appendix A. In the present flux scheme, the unknown post-streaming distribution functions can be directly calculated from the post-collision distribution functions and the prescribed flux constraint. Thus, the calculation of the normal derivative in flux $\mathbf{J}_\sigma$ with the finite difference method or boundary-neighboring nodes interpolation treatment can be avoided. Although the derivation of Eq. (14) in Appendix A utilizes the finite difference method, the implementation of this boundary scheme to calculate the unknown post-streaming distribution functions only involves boundary local nodes.

The very important step is to construct approximation equations for unknown distribution functions to close the system with multiple unknown variables, since Eq. (14) only provides one equation. One approximation method for unknown distribution functions was proposed by Yoshino and Inamuro [22]. In the present study, the same approximation method is adopted and test cases demonstrate that the approximation is still valid although the present boundary scheme removes the zero-flux assumption. On the boundary nodes, unknown distribution functions are approximated by Eq. (15) [22].

$$g_i=w_iC_w \quad \text{for } \mathbf{e}_i\cdot\mathbf{n}>0 \tag{15}$$

The approximation equation shown in Eq. (15) is actually the equilibrium distribution function for the concentration field shown in Eq. (9) with the fluid velocity term eliminated. It can be demonstrated that if the concentration field equilibrium distribution functions are used directly as approximation equations without eliminating the velocity term, the final result is the same as using reduced approximation equations shown in Eq. (15). Another approximation method to close the system was proposed in [28], which stated that the non-equilibrium portion of the distribution functions on the boundary are equal in magnitude but take on opposite signs in reverse directions.

The proposed flux boundary scheme is explained using a straight top boundary illustration in Fig. 1. The projection of the first-order moment of the distribution functions on the boundary normal **n** can be calculated following Eq. (14) and shown in Eq. (16).

$$\underbrace{-c\left(g_2^+ + g_5^+ + g_6^+\right)}_{\mathbf{c}_i\cdot\mathbf{n}\le 0} + \underbrace{c\left(g_4 + g_7 + g_8\right)}_{\mathbf{c}_i\cdot\mathbf{n}>0} = -J_y \tag{16}$$

In Eq. (16), the lattice speed $c = 1$, J_y is the flux magnitude through the top boundary. Substitute the approximate equations for g_4, g_7 and g_8 following Eq. (15) into Eq. (16), the wall concentration C_w can be calculated, as shown in Eq. (17).

$$C_w = \frac{J_y + \left(g_2^+ + g_5^+ + g_6^+\right)}{\left(w_4 + w_7 + w_8\right)} \tag{17}$$

The unknown post-streaming distribution functions g_4, g_7 and g_8 can be calculated by the approximation equation in Eq. (15) and the calculated wall concentration C_w in Eq. (17). From Eq. (14) and as discussed in Appendix A, the generalized calculation method for the wall concentration C_w can be given by Eq. (18).

$$C_w = \frac{\mathbf{J}\cdot\mathbf{n} - \sum_{\mathbf{e}_i\cdot\mathbf{n}\le 0} g_i^+ \mathbf{e}_i\cdot\mathbf{n}}{\sum_{\mathbf{e}_i\cdot\mathbf{n}>0} w_i\mathbf{e}_i\cdot\mathbf{n}} = \frac{\left(\mathbf{u}C - D\nabla C\right)\cdot\mathbf{n} - \sum_{\mathbf{e}_i\cdot\mathbf{n}\le 0} g_i^+ \mathbf{e}_i\cdot\mathbf{n}}{\sum_{\mathbf{e}_i\cdot\mathbf{n}>0} w_i\mathbf{e}_i\cdot\mathbf{n}} \tag{18}$$

The calculation of the wall concentration by Eq. (18), as well as the calculation of the unknown distribution functions by Eq. (15), shows that the present boundary scheme only involves boundary local nodes. Such a local boundary scheme is desirable in simulating transport processes in complex geometries, such as in porous media.

2.3. Flux scheme incorporating the rejection rate

The membrane mass rejection rate can be defined as $R_{ej} = (1–C_p/C_0) \times 100\%$, and in which C_p is the permeate water concentration, and C_0 is the feed water concentration. For a complete rejection membrane, the rejection rate $R_{ej} = 100\%$ since the permeate flux salinity $C_p = 0$. Usually the permeate flux (volumetric flux, with a unit of m s^{-1}) through the membrane can be measured, and salt ion mass flux (rate of mass flow per unit area, with a unit of kg s^{-1} m^{-2}) through the membrane can be treated as a convection process. Also, assume that the mass flux is constant through the membrane, and there is no accumulation of salts ions within the membrane. This assumption indicates a constant salt concentration and a negligible concentration gradient in the membrane. Since the concentration gradient is negligible through the membrane, the mass diffusion process is ignored and only the mass convection process is considered. Thus, based on former discussions, the mass flux boundary scheme incorporating the rejection rate can be designed and shown in Eq. (19).

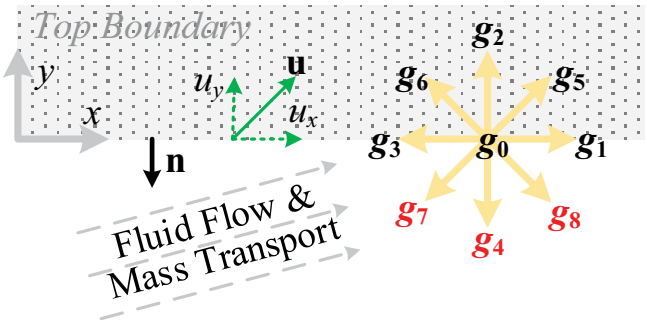

Fig. 1. Illustration of a Solid Top Boundary.

$$\begin{cases} C_w = \dfrac{\left[\mathbf{u}C\left(1\text{-}R_{ej}\right)\right]\cdot\mathbf{n} - \sum_{\mathbf{e}_i\cdot\mathbf{n}\le 0} g_i^+ \mathbf{e}_i\cdot\mathbf{n}}{\sum_{\mathbf{e}_i\cdot\mathbf{n}>0} w_i\mathbf{e}_i\cdot\mathbf{n}} \\ g_i = w_i C_w \quad \left(\mathbf{e}_i\cdot\mathbf{n} > 0\right) \end{cases} \tag{19}$$

3. Validation of the present flux boundary scheme

Cases with different types of flux boundary conditions are investigated to validate the present flux boundary scheme. These flux boundary conditions cover the general Neumann boundary (or the diffusive flux boundary), the zero normal derivative Neumann boundary (or the convective flux boundary), and the total flux boundary (or the convective plus diffusive flux boundary).

3.1. Neumann boundary

The Neumann boundary is used to prescribe the normal derivative of a variable on the boundary. A pure mass diffusion problem is invested with top and bottom boundary conditions shown in Eq. (20). The rectangular simulation domain $L \times H$ is prescribed with a Dirichlet boundary at the bottom boundary ($y = 0$) and a Neumann boundary at the top boundary ($y = H$). Both the left boundary ($x = 0$) and the right boundary ($x = L$) are periodic boundaries. Since it is a pure diffusion problem, there is no fluid flow through the simulation domain, that is, $\mathbf{u} = 0$ in Eq. (14). Also, from Eq. (20), the concentration derivative normal to the top boundary ($y = H$) varies sinusoidally along the horizontal boundary in x direction.

$$\begin{cases} C\left(x,y\right)\big|_{y=0} = C_0 \text{ (Dirichlet boundary)} \\ \left(\dfrac{\partial C\left(x,y\right)}{\partial y}\right)\Big|_{y=H} = C_s = \left|C_s\right|\sin\left(\beta x\right) \text{ (Neumann boundary)} \end{cases} \tag{20}$$

In Eq. (20), the wave number $\beta = \pi/24$. The system is analytically solvable and the exact solution of this problem is shown in Eq. (21) [18].

$$C\left(x,y\right) = C_0 + \frac{\left|C_s\right|\sin\left(\beta x\right)}{\beta}\frac{\sinh\left(\beta y\right)}{\cosh\left(\beta H\right)} \tag{21}$$

The height of the simulation domain $H = 20$, and the length of the simulation domain $L = 48$. The Dirichlet boundary condition is applied on the bottom boundary according to Eq. (5) with concentrations $C_0 = 1$ and $C_s = 0.01$ following

the study by Chen et al. [18]. All simulation parameters are in lattice units (dimensionless), and the conversion procedures between physical units and LBM units are shown in Appendix B. When the developed flux boundary scheme in Eq. (18) is applied on the top wall for the Neumann boundary, the calculated wall concentration can be shown in Eq. (22).

$$C_w = \frac{\left(\mathbf{u}C - D\nabla C\right)\cdot\mathbf{n} - \sum_{\mathbf{e}_i\cdot\mathbf{n}\le 0} g_i^+ \mathbf{e}_i\cdot\mathbf{n}}{\sum_{\mathbf{e}_i\cdot\mathbf{n}>0} w_i\mathbf{e}_i\cdot\mathbf{n}} = \frac{D|C_s|\sin(\beta x) + \left(g_2^+ + g_5^+ + g_6^+\right)}{\left(w_4 + w_7 + w_8\right)} \tag{22}$$

The simulation result can be expressed by the concentration distribution at five different horizontal positions (x = 1/4L, 3/8L, 1/2L, 5/8L, 3/4L) from the bottom wall to the top wall. Fig. 2 shows simulation results using different boundary schemes and indicates that the predicted concentration distribution using the present flux boundary scheme is identical to the result using the finite difference scheme, and both results match well with the analytical solution.

Besides the above pure diffusion case, a convection–diffusion process is tested for further validation. The fluid flow is added for the convection–diffusion transport with a Reynolds number Re = 10 and a Peclet number Pe = 10. For the flow field, a pressure-driven Poiseuille flow is assumed for the x direction (horizontal direction) velocity with a maximum value of u_{max} = 0.0833 with a lattice unit. The bottom boundary (y = 0) is a no-slip boundary and the top boundary is a velocity boundary with u_x = 0 and u_y = 0.001 with a lattice unit. The adoption of the velocity boundary u_y on the top boundary is intended for mass convection through the boundary. For the concentration field, all parameters and boundary conditions stay the same as in the pure diffusion case following Eq. (20). Thus, the top boundary (y = H) of the concentration field is a mass flux boundary involving both convection and diffusion. The left boundary (x = 0) and the right boundary (x = L) are periodic boundaries for both flow field and concentration field.

Concentration distributions at five different horizontal positions (x = 1/4L, 3/8L, 1/2L, 5/8L, 3/4L) from the bottom wall to the top wall with the finite difference scheme and the present flux scheme can be seen in Fig. 3. Results in the figure show that the present boundary scheme matches with the finite different scheme, and the total concentration in the simulation domain is reduced due to mass convection through the top boundary. However, at the top boundary, the concentration gradients at different horizontal positions are the same as the pure diffusion case because of the same constraint of Neumann boundary shown in Eq. (20).

3.2. Robin boundary

The Robin boundary is a weighted combination of the Dirichlet boundary and the Neumann boundary, which can be used to prescribe the total flux boundary composed of convection flux and diffusion flux. This validation case focuses on a time-dependent convection–diffusion problem in a two-dimensional domain $L \times H$ with constant mass flux as the input from the inlet (x = 0). For the concentration field, the detailed initial and boundary conditions can be described by Eq. (23). For the flow field, the inlet (x = 0) is a velocity boundary. The bottom boundary (y = 0) and the top boundary (y = H) of the simulation domain are symmetric boundaries for both the flow field and the concentration field.

$$\begin{cases} C(x,t)\big|_{t=0} = 0,\ 0 < x < L \ \text{(Initial condition)} \\ \left(\mathbf{u}C - D\dfrac{\partial C}{\partial \mathbf{n}}\right)\Big|_{x=0} = \mathbf{u}C_f,\ t > 0 \ \text{(Total flux boundary)} \\ \left(\dfrac{\partial C}{\partial \mathbf{n}}\right)\Big|_{x=L} = 0,\ t > 0 \ \text{(Zero normal derivative Neumann boundary)} \end{cases} \tag{23}$$

In Eq. (23), D = 0.01 m²/s, C_f = 50 mol/m³, and L = 1 m. The non-dimensional Peclet number Pe = $u_x L/D$ = 1 for this case. The constant value u_x at the velocity inlet boundary can be calculated using the Peclet number. The Neumann boundary defined in Eq. (23) at the outlet (x = L) indicates that there is no diffusion flux through this boundary. When

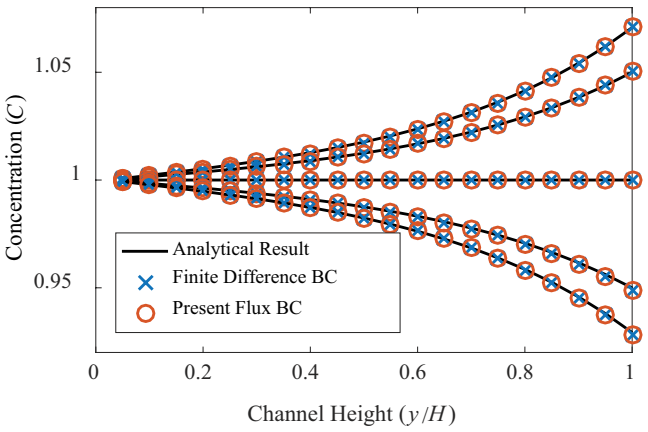

Fig. 2. Concentration distribution in pure diffusion.

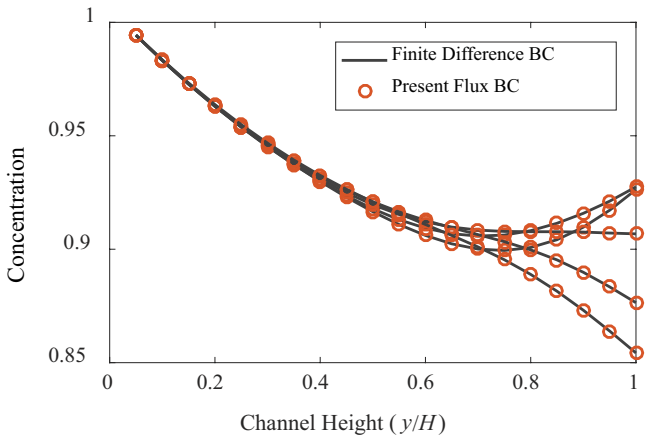

Fig. 3. Concentration distribution in convection–diffusion.

t is sufficiently small, the above problem has an asymptotic solution shown in Eq. (24) [17].

$$C(x,t)=C_f\left(\begin{array}{l}\frac{1}{2}\mathrm{erfc}\left(\frac{x-u_x t}{2\sqrt{Dt}}\right)+\sqrt{\frac{u^2 t}{\pi D}}\exp\left(-\frac{\left(x-u_x t\right)^2}{4Dt}\right)\cdots\\ \cdots-\frac{1}{2}\left(1+\frac{u_x x}{D}+\frac{u_x^2 t}{D}\right)\exp\left(\frac{u_x x}{D}\right)\mathrm{erfc}\left(\frac{x+u_x t}{2\sqrt{Dt}}\right)\end{array}\right) \quad (24)$$

In Eq. (24), exp is the exponential function and erfc is the complementary error function. The present flux boundary scheme Eq. (14) is used to prescribe the Robin boundary at the inlet (x = 0) and the Neumann boundary at the outlet (x = L). The simulation results of concentration distribution with the present flux boundary scheme matches well with the analytical asymptotic solution at different time spots, as seen in Fig. 4. These results show that the concentration on the left inlet boundary increases with time, and it is foreseeable that the concentration in the whole domain will finally reach C_f if the simulation time is long enough.

The accuracy of the boundary scheme is examined by the relative l^2-error norm vs. the mesh size. The relative error norm in the whole computational domain is defined with Eq. (25).

$$\mathrm{Er}=\frac{\sqrt{\sum_{x,y}\left(C_{\mathrm{num}}-C_{\mathrm{ana}}\right)^2}}{\sqrt{\sum_{x,y}C_{\mathrm{ana}}^2}} \quad (25)$$

The summation in Eq. (25) covers all nodes in the simulation domain. Concentrations C_{num} and C_{ana} denote the numerical value and the analytical solution, respectively. The simulation time t = 5 s, and four different concentration relaxation times τ_s = 0.05, 0.8, 1.0, 2.0 are selected for a better evaluation. For each relaxation time, eight different meshes with the x direction node number NX = 10, 20, 30, …, 80 are adopted. The relative error calculation results are shown in Fig. 5, which indicates that the new numerical scheme has a convergence order of 1. The convergence order evaluation is within expectations since the approximation equations for the unknown distribution functions in Eq. (15) are first order. A higher convergence order, if desirable, may be achieved with a higher order algorithm as a replacement of Eq. (15), but it is beyond the scope of the current paper as a pioneer of this type of flux boundary scheme.

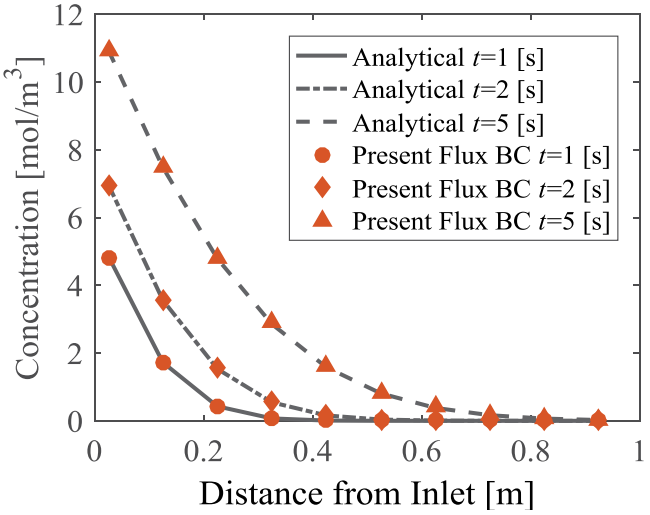

Fig. 4. Transient concentration in different simulation durations.

3.3. Reaction boundary

To further validate the proposed flux boundary scheme, a reaction boundary in a rectangular domain is selected and for which there exists an analytic solution. The simulation domain is rectangular with the length and the height as $L \times H$. Refer to Fig. 6 and Eq. (26), the reaction takes place at the top boundary (y = H) with first-order linear kinetics, which is actually a Neumann boundary. At the bottom boundary (y = 0) and the right boundary (x = L), zero concentration gradient normal to the boundary is specified. Solute is allowed to diffuse into the domain from the left boundary (x = 0), thus there should be a Dirichlet boundary condition (C = C_0) specified there.

$$\left\{\begin{array}{l}C(0,y)=C_0;\ \left.\frac{\partial C}{\partial x}\right|_{x=L}=0;\ \left.\frac{\partial C}{\partial y}\right|_{y=0}=0\\ -D\left.\frac{\partial C}{\partial y}\right|_{y=H}=k_r\left(C|_{y=H}-C_{\mathrm{eq}}\right)\end{array}\right. \quad (26)$$

In Eq. (26), the reaction rate k_r = 0.1, the diffusion coefficient D = 1/6, the equilibrium concentration C_{eq} = 1, the inlet concentration C_0 = 10, the length of the simulation domain L = 100, and the height of the simulation domain H = 80 (all parameters are dimensionless). The analytical solution for $C(x,y)$ can be obtained by separation of variables, as shown in Eq. (27) [29].

$$C(x,y)=C_{\mathrm{eq}}+\left(C_0-C_{\mathrm{eq}}\right)\sum_{n=1}^{\infty}\frac{\sin\left(\beta_n H\right)}{N_n^2\beta_n}\frac{\cosh\left[\beta_n\left(x-L\right)\right]}{\cosh\left(\beta_n L\right)}\cos\left(\beta_n y\right) \quad (27)$$

In Eq. (27),

$$N_n^2=\frac{H}{2}\left(1+\frac{\sin\left(2\beta_n H\right)}{2\beta_n H}\right) \quad (28)$$

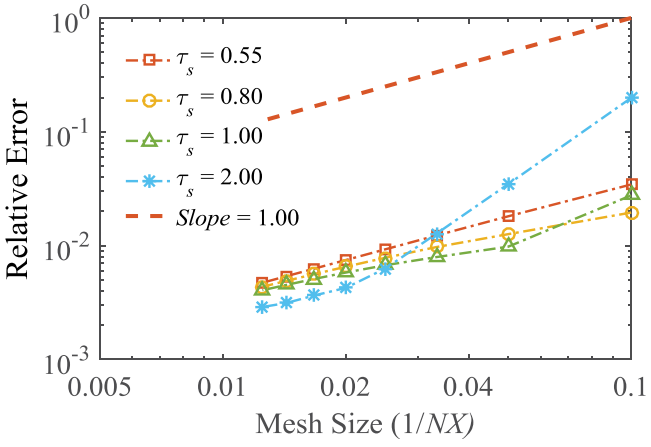

Fig. 5. Relative error vs. mesh size in the Robin boundary case.

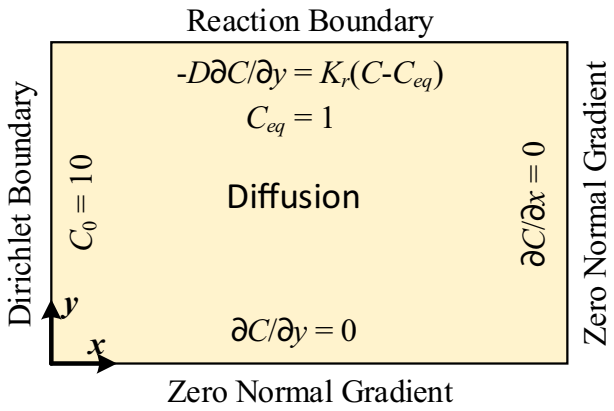

Fig. 6. Illustration of boundary conditions in the reaction boundary case.

The variable β_n in Eqs. (27) and (28) can be determined from the transcendental equation by Eq. (29).

$$(\beta_n H)\tan(\beta_n H) = \frac{k_r H}{D} \tag{29}$$

The left Dirichlet boundary is prescribed using Eq. (5), the right and the bottom zero normal gradient boundaries are prescribed using the present boundary scheme in Eq. (14). Two boundary schemes are used on the top reaction boundary for comparison purpose, Kang et al.'s [28] (improved) reaction boundary scheme and the present flux boundary scheme Eq. (14). The analytical result as well as the simulation results for the solute concentration at steady state is shown in Fig. 7. From the figure, we can see that near the top reaction boundary, simulation result by the present flux boundary scheme matches better with analytical result.

The accuracy of the boundary scheme is examined by the relative l^2-error norm vs. the mesh size following Eq. (25). Two reaction rates are selected as k_r = 0.1 and 0.01. For each

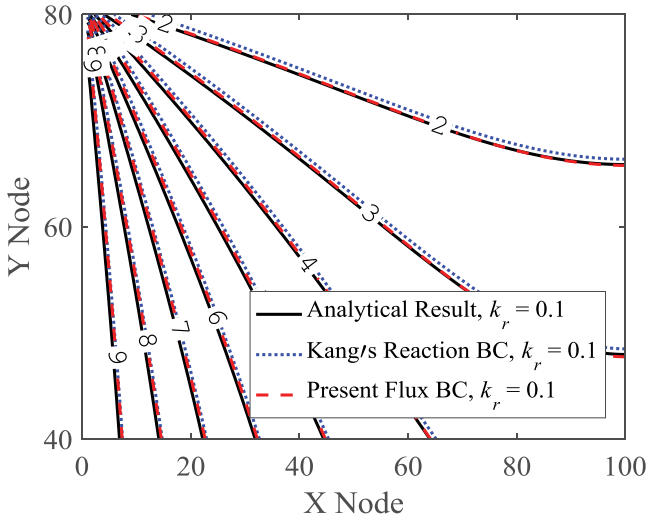

Fig. 7. Contours of solute concentration at steady state.

reaction rate, seven different mesh plans with y direction node number NY = 40, 60, 80, 100, 120, 140, 160 are adopted. The relative error calculation results are shown in Fig. 8, which indicates that although both Kang et al.'s [28] reaction boundary scheme and the present flux boundary scheme have an accuracy order of 1, the present flux boundary scheme has lower relative error for both of the reaction rates.

4. Application of the present flux boundary scheme

4.1. Treatment of the large Peclet number problem

In many mass transport cases, small particles such as ions in dilute solution have a very small diffusion coefficient. For example, the self-diffusion coefficients of the five major ions in seawater at 25°C are all in the order of 1×10^{-9} m^2/s [30]. Following the conversion procedures shown in Appendix B between lattice units and physical units, the solute relaxation time can be calculated by using Eq. (30).

$$D_{\mathrm{LBM}} = \frac{\left(\tau_s - \frac{1}{2}\right)c^2\delta t}{3} \xrightarrow{c=1,\delta t=1} \tau_s = 3D_{\mathrm{LBM}} + \frac{1}{2} \tag{30}$$

The diffusion coefficient D_{LBM} with a lattice unit in Eq. (30) can be calculated from the diffusion coefficient $D_{\mathrm{PHY}} = 1.5 \times 10^{-9}$ m^2/s with a physical unit. Then the calculated relaxation time τ_s = 0.5008, which is actually near the instability value of 0.5 in LBM [16]. Sometimes, in a coupled simulation of the Navier–Stokes equations and the convection–diffusion equation, the correlation between the fluid field relaxation time τ and the concentration field relaxation time τ_s should be strictly controlled to accurately represent the ratio of convective mass transfer to diffusive mass transport. The Peclet number is defined to be the ratio of advection by the flow for a physical quantity to the rate of diffusion by an appropriate gradient, as shown in Eq. (31).

$$\mathrm{Pe} = \frac{L \cdot u}{D} = \frac{L \cdot u}{\nu} \cdot \frac{\nu}{D} = \mathrm{Re} \cdot \mathrm{Sc} \tag{31}$$

In Eq. (31), L is the characteristic length, u is the local flow velocity, D is the mass diffusion coefficient, ν is the kinematic viscosity, and Sc is the Schmidt number. Take seawater for example, the kinematic viscosity is $\nu = 1 \times 10^{-6}$ m^2/s, and the calculated Schmidt number is Sc ≈ 667. From Eq. (31), for a channel flow with Re = 100, the calculated Peclet number Pe ≈ 66700. In a mass transport process with such a large Peclet number, the mass diffusion can actually be ignored in the fluid flow direction in the membrane filtration channel since mass convection is dominant. However, in other cases, such as mass transport in membrane filtration, although bulk flow mass transport is convection dominant, boundary layer mass transport is not necessarily convection dominant. Mass diffusion would play an important role near the boundary layer since permeate flow induced convection through the membrane is comparable with the concentration gradient induced back diffusion. Thus, the coupled simulation of such a complex convection–diffusion process is challenging with a regular LBM routine.

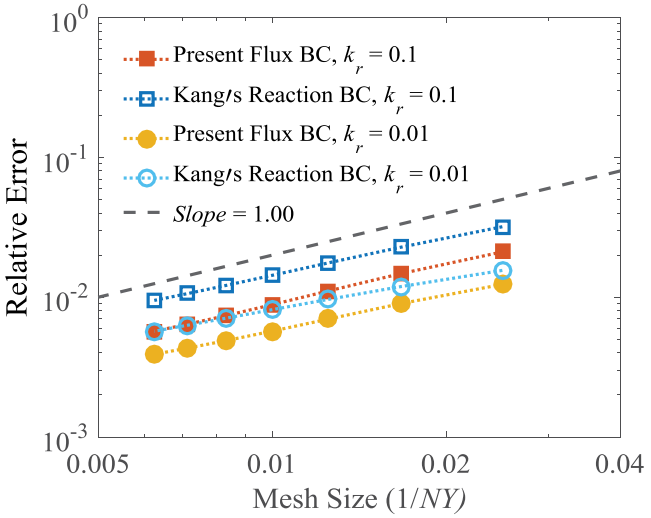

Fig. 8. Relative error vs. mesh size in the reaction boundary case.

Perko and Patel [31] developed an effective lattice Boltzmann scheme to deal with the instability problem featuring large diffusion-coefficient heterogeneities and high-advection in convection diffusion processes. The basic idea is to divide the physical diffusion coefficient into a reference value D_{ref}, which is constant over the entire domain, and a fluctuating or residue value $\hat{D}$, which represents a deviation from the reference ($D = D_{ref} + \hat{D}$). Then, the fluctuating diffusion part is transferred to the advection term by introducing a diffusion velocity $\mathbf{u}_d$, as shown in Eq. (32).

$$\mathbf{J} = \mathbf{u}C - \left(D_{ref} + \hat{D}\right)\nabla C = -D_{ref}\nabla C + \left(\mathbf{u} + \mathbf{u}_d\right)C \tag{32}$$

In Eq. (32), the diffusion velocity can be calculated by Eq. (33).

$$\mathbf{u}_d = -\frac{\hat{D}\nabla C}{C} \tag{33}$$

For a transport process with a very small diffusion coefficient and a very large Peclet number, such as in the seawater desalination, the reference diffusion coefficient can be selected to be a large value for a better numerical stability, and then the calculated residue fluctuating diffusion part should be negative. A validation case is adopted to investigate the feasibility of the present boundary scheme in the application of the Peclet number transport process.

This validation case focuses on a pure mass diffusion process in a simulation domain comprised of three regions, as seen in Fig. 9. The first and last 2 cm regions have a very small diffusion coefficient D_{low} = 1 × 10^{-11} m²/s, while the middle 0.06 m region has a much larger diffusion coefficient D_{high} = 2,000D_{low}. The reference diffusion coefficient is selected to be D_{low} for the whole domain. The initial concentration $C(x,t_0)$ = 0.1 mol/m³. The left boundary of the simulation domain is prescribed with a constant concentration as a Dirichlet boundary, and the right boundary is a zero diffusive flux Neumann boundary (zero gradient normal to the boundary). Symmetric boundaries are assumed to the top and the bottom boundaries. Simulation time is selected to be

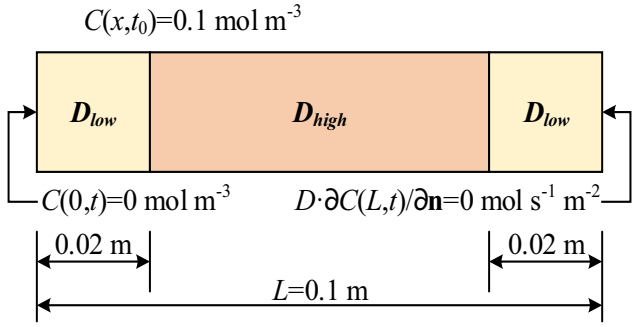

Fig. 9. Pure diffusion with spatially variable diffusion coefficients.

500 d. The reference solution was obtained in reference [31] using the commercial FEM-based COMSOL Multiphysics software.

Simulation results of the present flux boundary scheme, as well as the finite difference boundary scheme are compared with the reference solution as shown in Fig. 10. Well match of results from a variety of numerical methods and boundary schemes demonstrates the feasibility of the present flux boundary scheme in the simulation of large Peclet number process, which lays a foundation for the applications of the present flux boundary scheme in the CP prediction and the inorganic fouling growth simulation.

4.2. CP predictions in the seawater desalination

Pressure-driven RO seawater desalination is a convection dominant large Peclet number process since the diffusion coefficient of salt ions in the feed flow is extremely small (in an order of 10^{-9} m²/s). First, the zero-flux boundary is prescribed on membrane boundaries located at the top and the bottom of the desalination channel, which means there is no mass flux through the membrane and all salt ions are rejected by the membrane. The desalination channel height H = 1 mm (in y direction) and the channel length L = 1 cm (in x direction). The width of the channel is assumed to be sufficiently large in spanwise direction (in z direction), and thus a 2D simulation domain is targeted to represent the desalination channel. The transmembrane permeate flux $v_w = P_{er}(\Delta P - \Delta\pi)$ as given by Li et al. [32], in which P_{er} = 7.3 × 10^{-12} m/(s × Pa) is a permeability constant of the RO membrane, ΔP = 5.5 × 10^6 Pa is the transmembrane pressure, and $\Delta\pi$ is the osmotic pressure between the feed side and the permeate side of the RO membrane. The concentration for the feed seawater C_0 = 32,000 mg/L, the diffusion coefficient for salt ions in the feed seawater D = 1.5 × 10^{-9} m²/s. The pressure gradient for the feed flow in the desalination channel dP/dx = –800 Pa/m.

A bounce-back scheme in LBM is used to prescribe the zero-flux boundary for a comparison purpose. The bounce-back scheme is usually used to prescribe the zero-flux boundary when solving the convection–diffusion equation to mimic the non-slip boundary condition in solving the NS equations [33]. All simulation parameters have same values with those in the published FEM benchmark case [34]. Simulation results of the CP and permeate flux, as well as published benchmark results [34], are shown in Fig. 11.

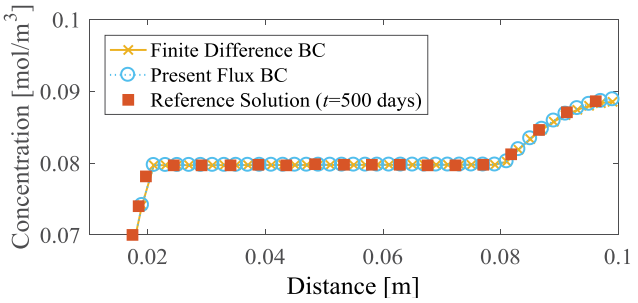

Fig. 10. Concentration in the diffusion-coefficient heterogeneity case.

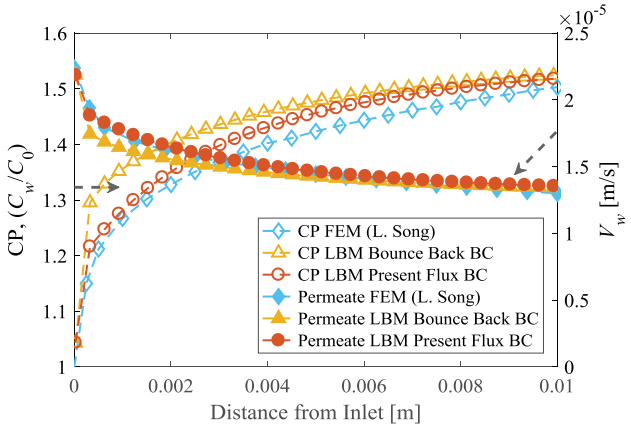

Fig. 11. CP and permeate flux in a plain channel.

Fig. 11 shows that results from the present flux boundary scheme match better than the bounce-back scheme with the published FEM results especially at the vicinity of the inlet. For the bounce-back scheme, the post-streaming distribution functions are calculated using the post-collision distribution functions in the collinear opposite directions only (along the link direction). This means all mass particles are bounced back without any slip at the membrane boundary. However, the no-slip constraint is released in the present flux boundary scheme, in which the post-collision distribution functions in multiple non-collinear directions are accounted to calculate the post-streaming distribution functions. Since the no-slip constraint of the bounce-back boundary scheme delays the moving of the near boundary particles toward the downstream, the predicted CP near the inlet is higher than that using the present flux boundary scheme. While far from the inlet and near the steady state CP region, the difference vanishes for the two schemes. This can explain the better match of present flux boundary scheme near the inlet region shown in Fig. 11.

The concentration distribution on the cross section at the middle position of the channel length is plotted in Fig. 12. From Fig. 12, the CP boundary layer thicknesses are almost same for both of the LBM zero-flux boundary schemes, which are about 0.07 mm.

The CP prediction with the membrane salt rejection rate varying from 50% to 100% can be performed by applying the mass flux boundary scheme coupled with the rejection rate as shown in Eq. (19). Prediction results shown in Fig. 13

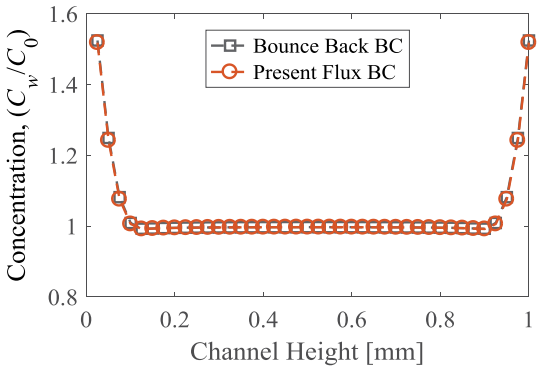

Fig. 12. Concentration at the channel middle cross-section in different boundary schemes.

indicate that the CP is lower with a lower membrane rejection rate, since more salt ions will be transported through the membrane in a lower rejection rate situation and thus less amount of salt ions can be accumulated near the membrane. Also, permeate flux prediction results in Fig. 13 show that the membrane designed for higher salt rejection has lower permeate flux. This conclusion means that a trade-off exists between the membrane selectivity (salt rejection) and the membrane permeability (permeate flux), as reported by Park et al. [35] that highly permeable membranes lack the selectivity and vice versa. Detailed review and discussion about the permeability–selectivity trade-off for synthetic membranes can be seen in the study by Park et al. [35].

The CP boundary layer thickness is almost invariant with different salt rejection rates, as can be seen in Fig. 14.

4.3. Fouling growth in the seawater desalination

The present boundary scheme is also easily applicable for curved boundaries with staircase approximations. In this section, the developed boundary scheme is applied to study inorganic fouling growth on the membrane surface in seawater desalination.

Inorganic fouling growth is often a slow kinetic process, and the development of fouling mitigation strategies typically relies on thermodynamic solubility calculations and experimental trial and error. In this study, the growth simulation of a gypsum crystal as representative inorganic fouling is targeted. The fouling growing model on the membrane surface as well as gypsum growth kinetics in the LBM framework was discussed by the researchers of the present study in a former publication [36]. Gypsum growth kinetics depends highly on the solute concentration around growing fouling. Thus, the curved boundary condition at the fluid–solid interface is critical in simulating the fouling size and fouling morphology. In this fouling growth simulation, the first-order kinetic-reaction model [37] shown in Eq. (34) is used at the fluid-fouling interface.

$$D\frac{\partial C}{\partial \mathbf{n}} = k_r\left(C - C_s\right) \tag{34}$$

In Eq. (34), the diffusivity $D = 1.5 \times 10^{-9}$ m^2/s, which is the same as the diffusivity used in the CP model, C is the solute concentration at the interface, C_s is the solute saturation

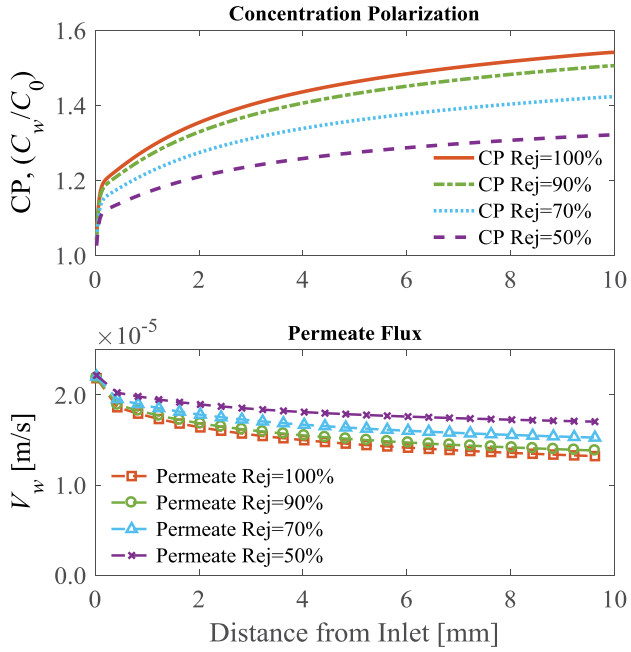

Fig. 13. CP prediction with different rejection rates.

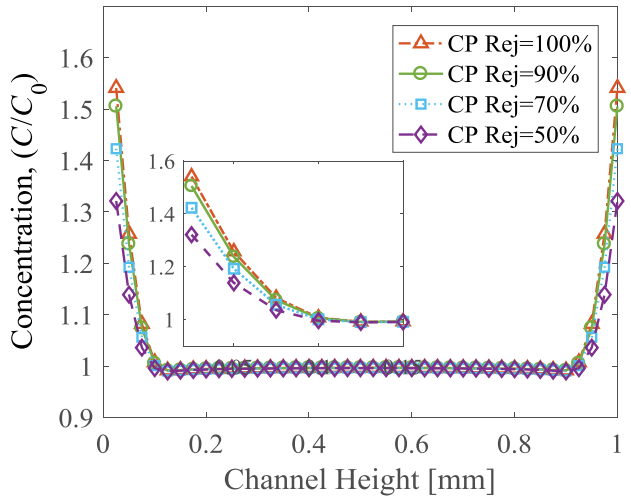

Fig. 14. Concentration at the channel middle cross-section in different rejection rates.

concentration, k_r is the local reaction-rate constant, and **n** is the direction normal of staircase boundary pointing toward the fluid phase. From gypsum growth kinetics [36], the local reaction-rate constant k_r is equal to the mass transfer coefficient (k_m = 2.949 × 10^{-5} m/s) for a diffusion-controlled crystallization process. The saturation concentration C_s of calcium sulfate is calculated to be 2.071 kg/m^3 at a given temperature 25°C [36]. The concentration of $CaSO_4$ in seawater near the membrane surface C_w = SI × C_s, in which SI is the supersaturation ratio. The gypsum crystal growth simulation is performed with a supersaturation ratio of 2.

From Eq. (14) and discussions in Appendix A, the term ($-D\partial C/\partial \mathbf{n}$) is diffusion flux flowing out of the solid phase toward the fluid phase, thus the term ($D\partial C/\partial \mathbf{n}$) on the left-hand side of Eq. (34) represents reaction flux of the gypsum ions from the fluid phase to the solid phase to provide ions for continuous nucleation and crystallization. In a previous publication [36], the curved reaction boundary was prescribed using Kang et al.'s [37] reactive transport method. In this paper, the proposed mass flux boundary scheme is used to prescribe the reaction boundary.

The implementation of the present boundary scheme is illustrated in Fig. 15. In the figure, the rosette structure of the surface gypsum crystal is illustrated by a circular structure, which is then numerically approximated by zig-zag staircases. Indicators will be defined to find and mark different types of cells in the simulation domain.

All staircase edges at the interface between the solid boundary cell and the fluid boundary cell are reaction edges and applied with the reaction boundary shown in Eq. (34). Substitution of the reaction boundary Eq. (34) into the present boundary scheme Eq. (14) yields Eq. (35).

$$\underbrace{\sum_{\mathbf{e}_i\cdot\mathbf{n}>0} g_i\mathbf{e}_i\cdot\mathbf{n}}_{\text{unkonwn}} + \underbrace{\sum_{\mathbf{e}_i\cdot\mathbf{n}\le 0} g_i^{+}\mathbf{e}_i\cdot\mathbf{n}}_{\text{konwn}} = \left(\mathbf{u}C - D\nabla C\right)\cdot\mathbf{n} = \left(\mathbf{u}\cdot\mathbf{n}\right)C - k_r\left(C - C_s\right) \tag{35}$$

Eq. (35) indicates that there is always a negative sign on the term $k_r(C - C_s)$ at reaction edges with different unit normal vectors **n**. This means that reaction mass flux is always in the opposite direction of the unit normal vector **n**, and flows from the fluid phase toward the solid phase.

Simulation results of crystal size and mass accumulation using the present boundary scheme and Kang et al.'s [37] reaction boundary are shown in Fig. 16. The dashed cross-lines in Fig. 16 show the initial nucleation positions, which clearly indicate that the crystals are more prone to grow in the opposite direction of the feed flow (flow direction is from left to right). This conforms to experimental observations [38] and the previous numerical study [36], in which growth of gypsum crystals is more prone in the direction opposite to that of the feed flow.

This axially asymmetric growth of the gypsum crystal could be explained by concentration simulation results as shown in Fig. 17. The salt concentration decreases from the crystal frontal flow-stagnation edge to the rear of the crystal, and a higher concentration induces faster growth of the crystal toward the direction opposite to the feed flow. The reduced calcium sulfate concentration downstream of the

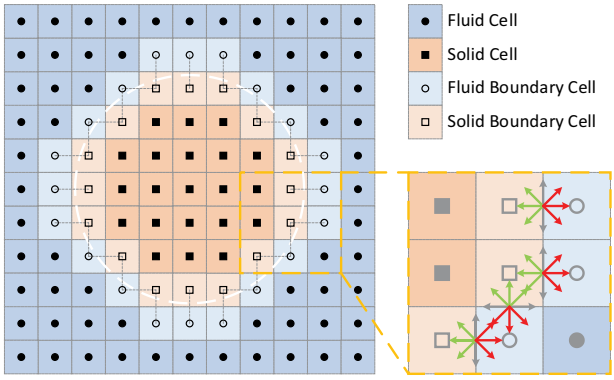

Fig. 15. Illustration of the crystal structure and its staircase approximation.

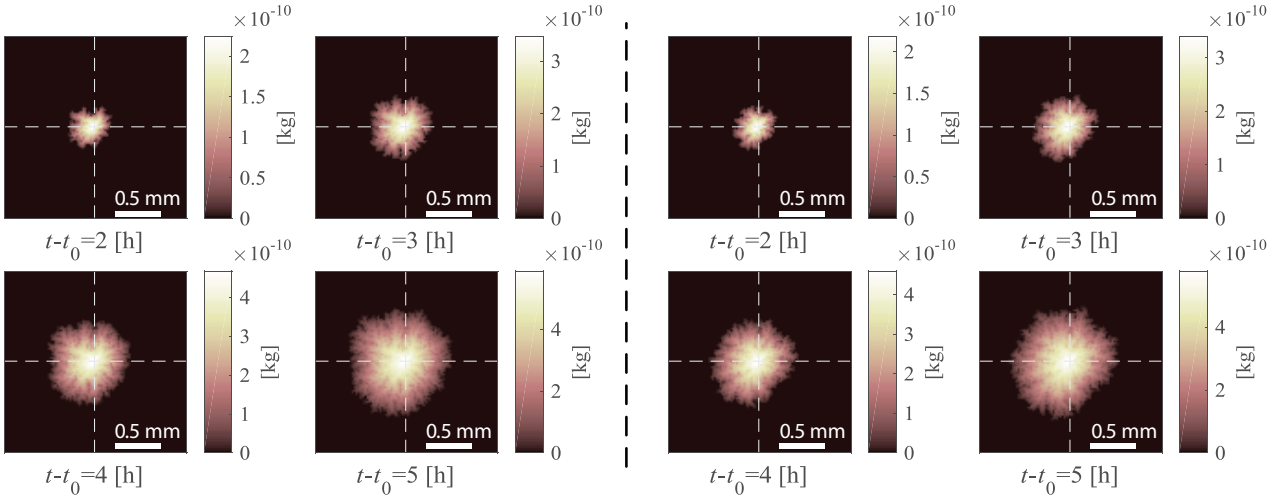

Fig. 16. Crystal size and mass accumulation: present scheme (left) and Kang et al.'s [37] scheme (right).

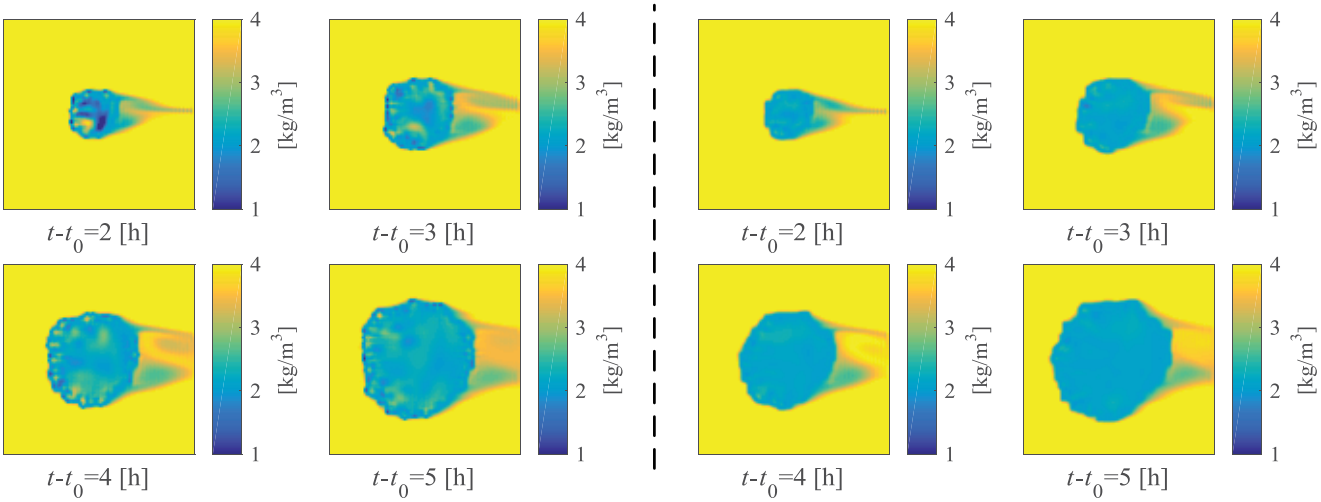

Fig. 17. Field concentration: present scheme (left) and Kang et al.'s [37] scheme (right).

crystal results from mixing eddies caused by the abrupt obstacle of the growing non-permeation crystal. Gypsum crystallization gradually consumes salt ions around the crystal, thus the salt concentration layer around the crystal is lower than the concentration in the bulk flow.

Using both of the present boundary scheme and Kang et al.'s [37] reaction scheme, the equivalent radii of fouling crystals are 0.190, 0.286, 0.381 and 0.475 mm, for the growing time of 2, 3, 4 and 5 h, respectively. Inorganic fouling growth simulation results in Figs. 16 and 17 show that when used to prescribe the reaction boundary condition in Eq. (34), the present boundary scheme agrees well with Kang et al.'s [37] reaction scheme in terms of the crystal size, mass accumulation and concentration distribution around the fouling crystal. Implementation procedures of the present boundary scheme in staircase approximated curve boundaries are actually identical with those in straight boundaries. Thus, the present boundary scheme has a first-order accuracy for curved boundaries.

5. Conclusions

Pressure-driven membrane filtration is the most common method for saltwater desalination and wastewater treatment. The inherent CP phenomenon in membrane desalination plays a vital role in triggering surface fouling, as it leads to elevated solute concentration near the membrane surface. A simple and effective flux boundary scheme is proposed and validated in this study, which only involves the boundary local nodes without utilizing the finite difference approximation or the boundary-neighboring nodes interpolation.

The proposed flux boundary scheme is applied to predict the CP and to simulate fouling growth in seawater desalination. The CP and permeate flux prediction result from LBM agrees well with the FEM benchmark case in a complete rejection condition. With the removal of the complete rejection assumption and with the rejection rate considered, the CP is reduced with a lower rejection rate,

since more salt ions would be transported through the membrane and accumulated salt ions would be reduced. A higher CP and lower permeate flux in a larger rejection rate condition indicate a trade-off between membrane selectivity (salt rejection) and membrane permeability (permeate flux). Also, prediction results show that the CP boundary layer thickness is almost invariant with different salts rejection rates. Results of the inorganic fouling growth simulation agree well with reported results in terms of the crystal size, mass accumulation and concentration distribution. The fouling growth simulation case shows that the present boundary scheme is valid for curved boundaries with staircase approximations.

Validation and application cases demonstrate the feasibility of the proposed flux boundary scheme in a variety of boundary conditions. The present flux boundary scheme accounts for the post-collision distribution functions in multiple non-collinear directions. This differs from existing boundary schemes using post-collision distribution functions only in collinear directions (same or opposite directions), such as the bounce-back scheme [34], Kang et al.'s [37] reaction scheme and interpolation schemes [17]. This may explain the better match of the present boundary scheme with the reference data than adopted popular boundary schemes in some cases, such as the validation case in section 3.3 and the application case in section 4.2. The proposed flux boundary scheme has a first-order accuracy for both straight boundaries and curved boundaries, and future work may include developing a second-order accuracy flux boundary scheme.

Symbols

- $\mathbf{J}$ — Heat flux or mass flux, W/m^2 or kg/(m^2 s)
- f_i — Particle distribution functions for the fluid field
- g_i — Particle distribution functions for the thermal/concentration field
- $\mathbf{e}_i$ — Discrete velocities for the particle distribution functions
- w_i — Weight coefficients for the particle distribution functions
- $\mathbf{n}$ — Unit normal vector on the boundary, pointing toward the interior of the domain
- c_s — Lattice sound speed, dimensionless
- τ — Relaxation time for the fluid flow lattice Boltzmann equations
- τ_s — Relaxation time for the mass transport lattice Boltzmann equations
- $\mathbf{u}$ — Fluid velocity vector, m/s
- C — Species concentration, kg/m^3 or g/L
- ν — Kinematic viscosity ($\nu = \mu/\rho$), m^2/s
- μ — Absolute or dynamic viscosity, (N s/m^2) or kg/(m s)
- ρ — Fluid or solution density, kg/m^3
- D — Mass transport diffusion coefficient (mass diffusivity), m^2/s
- Re — Reynolds number, Re = uL/ν
- Pe — Peclet number, Pe = uL/D
- Sc — Schmidt number, Sc = ν/D
- $\mathbf{u}_d$ — Diffusion velocity, m/s
- P_{er} — Water permeability constant, m/(s×Pa)
- v_w — Transmembrane permeate flux normal to the membrane boundary, m/s

Acknowledgment

The authors would like to acknowledge the financial support from the Qatar National Research Fund (No.: 6-213-2-090, Centrifugal Pressure - Vibrating Membrane Reverse Osmosis Desalination and Fracking Waste Water Recovery).

References

[1] A. Al-Karaghouli, L.L. Kazmerski, Energy consumption and water production cost of conventional and renewable-energy-powered desalination processes, Renewable Sustainable Energy Rev., 24 (2013) 343–356.
[2] A.L. Zydney, Stagnant film model for concentration polarization in membrane systems, J. Membr. Sci., 130 (1997) 275–281.
[3] D. Bhattacharyya, S.L. Back, R.I. Kermode, M.C. Roco, Prediction of concentration polarization and flux behavior in reverse osmosis by numerical analysis, J. Membr. Sci., 48 (1990) 231–262.
[4] E. Lyster, Y. Cohen, Numerical study of concentration polarization in a rectangular reverse osmosis membrane channel: permeate flux variation and hydrodynamic end effects, J. Membr. Sci., 303 (2007) 140–153.
[5] A.L. Ahmad, K.K. Lau, M.Z.A. Bakar, S.R.A. Shukor, Integrated CFD simulation of concentration polarization in narrow membrane channel, Comput. Chem. Eng., 29 (2005) 2087–2095.
[6] W. Zhang, J. Luo, L. Ding, M.Y. Jaffrin, A review on flux decline control strategies in pressure-driven membrane processes, Ind. Eng. Chem. Res., 54 (2015) 2843–2861.
[7] S.Y. Chen, D. Martinez, R.W. Mei, On boundary conditions in lattice Boltzmann methods, Phys. Fluids., 8 (1996) 2527–2536.
[8] C.K. Aidun, J.R. Clausen, G.W. Woodruff, Lattice-Boltzmann method for complex flows, Annu. Rev. Fluid Mech., 42 (2010) 439–472.
[9] J. Zhang, Lattice Boltzmann method for microfluidics: models and applications, Microfluid. Nanofluid., 10 (2011) 1–28.
[10] Y. Chen, Q. Cai, Z. Xia, M. Wang, S. Chen, Momentum-exchange method in lattice Boltzmann simulations of particle-fluid interactions, Phys. Rev. E., 88 (2013) 013303.
[11] S.D.C. Walsh, M.O. Saar, Macroscale lattice-Boltzmann methods for low Peclet number solute and heat transport in heterogeneous porous media, Water Resour. Res., 46 (2010) 1–15.
[12] Q. Kang, D. Zhang, S. Chen, X. He, Lattice Boltzmann simulation of chemical dissolution in porous media, Phys. Rev. E., 65 (2002) 036318.
[13] S. Anwar, M.C. Sukop, Lattice boltzmann models for flow and transport in saturated karst, Groundwater, 47 (2009) 401–413.
[14] J. Kromkamp, A. Bastiaanse, J. Swarts, G. Brans, R.G.M. Van Der Sman, R.M. Boom, A suspension flow model for hydrodynamics and concentration polarisation in crossflow microfiltration, J. Membr. Sci., 253 (2005) 67–79.
[15] D.A.G. Von Der Schulenburg, T.R.R. Pintelon, C. Picioreanu, M.C.M. Van Loosdrecht, M.L. Johns, Three-dimensional simulations of biofilm growth in porous media, AIChE J., 55 (2009) 494–504.
[16] T. Zhang, B. Shi, Z. Guo, Z. Chai, J. Lu, General bounce-back scheme for concentration boundary condition in the lattice-Boltzmann method, Phys. Phys. Rev. E., 85 (2012) 016701.
[17] J. Huang, W.-A. Yong, Boundary conditions of the lattice Boltzmann method for convection–diffusion equations, J. Comput. Phys., 300 (2015) 70–91.
[18] Q. Chen, X. Zhang, J. Zhang, Improved treatments for general boundary conditions in the lattice Boltzmann method for convection-diffusion and heat transfer processes, Phys. Rev. E., 88 (2013) 033304.
[19] L. Li, R. Mei, J.F. Klausner, Boundary conditions for thermal lattice Boltzmann equation method, J. Comput. Phys., 237 (2013) 366–395.
[20] I. Ginzburg, Generic boundary conditions for lattice Boltzmann models and their application to advection and anisotropic dispersion equations, Adv. Water Resour., 28 (2005) 1196–1216.

[21] P.H. Kao, R.J. Yang, An investigation into curved and moving boundary treatments in the lattice Boltzmann method, J. Comput. Phys., 227 (2008) 5671–5690.
[22] M. Yoshino, T. Inamuro, Lattice Boltzmann simulations for flow and heat/mass transfer problems in a three-dimensional porous structure, Int. J. Numer. Methods Fluids, 43 (2003) 183–198.
[23] Z. Guo, T.S. Zhao, Lattice Boltzmann model for incompressible flows through porous media, Phys. Rev. E., 66 (2002) 036304.
[24] S. Chen, G. Doolen, Lattice Boltzmann Method for Fluid Flows, Annu. Rev. Fluid Mech., 30 (1998) 329–364.
[25] R. Huang, H. Wu, A modified multiple-relaxation-time lattice Boltzmann model for convection-diffusion equation, J. Comput. Phys., 274 (2014) 50–63.
[26] Z. Chai, T.S. Zhao, Lattice Boltzmann model for the convection-diffusion equation, Phys. Rev. E, 87 (2013) 063309.
[27] H. Yoshida, M. Nagaoka, Multiple-relaxation-time lattice Boltzmann model for the convection and anisotropic diffusion equation, J. Comput. Phys., 229 (2010) 7774–7795.
[28] Q. Kang, P.C. Lichtner, D. Zhang, An improved lattice Boltzmann model for multicomponent reactive transport in porous media at the pore scale, Water Resour. Res., 43 (2007) 1–12.
[29] Q. Kang, P.C. Lichtner, D. Zhang, Lattice Boltzmann pore-scale model for multicomponent reactive transport in porous media, J. Geophys. Res. Solid Earth., 111 (2006) 1–12.
[30] A. Poisson, A. Papaud, Diffusion coefficients of major ions in seawater, Mar. Chem., 13 (1983) 265–280.
[31] J. Perko, R.A. Patel, Single-relaxation-time lattice Boltzmann scheme for advection-diffusion problems with large diffusion-coefficient heterogeneities and high-advection transport, Phys. Rev. E., 89 (2014) 053309.
[32] W. Li, X. Su, A. Palazzolo, S. Ahmed, E. Thomas, Reverse osmosis membrane, seawater desalination with vibration assisted reduced inorganic fouling, Desalination, 417 (2017) 102–114.
[33] H.-B. Huang, X.-Y. Lu, M.C. Sukop, Numerical study of lattice Boltzmann methods for a convection–diffusion equation coupled with Navier–Stokes equations, J. Phys. A: Math. Theor., 44 (2011) 055001.
[34] L. Song, S. Ma, Numerical studies of the impact of spacer geometry on concentration polarization in spiral wound membrane modules, Ind. Eng. Chem. Res., 44 (2005) 7638–7645.
[35] H.B. Park, J. Kamcev, L.M. Robeson, M. Elimelech, B.D. Freeman, Maximizing the right stuff: the trade-off between membrane permeability and selectivity, Science, 356 (2017) 1138–1148.
[36] W. Li, X. Su, A. Palazzolo, S. Ahmed, Numerical modeling of concentration polarization and inorganic fouling growth in the pressure-driven membrane filtration process, J. Membr. Sci., 569 (2019) 71–82.
[37] Q. Kang, D. Zhang, P.C. Lichtner, I.N. Tsimpanogiannis, Lattice Boltzmann model for crystal growth from supersaturated solution, Geophys. Res. Lett., 31 (2004) 1–5.
[38] M. Uchymiak, E. Lyster, J. Glater, Y. Cohen, Kinetics of gypsum crystal growth on a reverse osmosis membrane, J. Membr. Sci., 314 (2008) 163–172.

Appendix A. Derivation of the flux boundary scheme

Since curved boundaries can be approximated by zig-zag staircases, a straight boundary will be used for the illustrating the derivation process. Substituting concentration distribution functions (in post-streaming form) on the top boundary illustrated in Fig. A1 into Eq. (13) yields Eq. (A1).

$$\frac{\delta y}{\delta t}\underbrace{\left(g_2+g_5+g_6\right)}_{\text{known}}-\frac{\delta y}{\delta t}\underbrace{\left(g_4+g_7+g_8\right)}_{\text{unknown}}=u_y C-\frac{\tau}{3}\frac{\delta y^2}{\delta t}\frac{\partial C}{\partial y} \tag{A1}$$

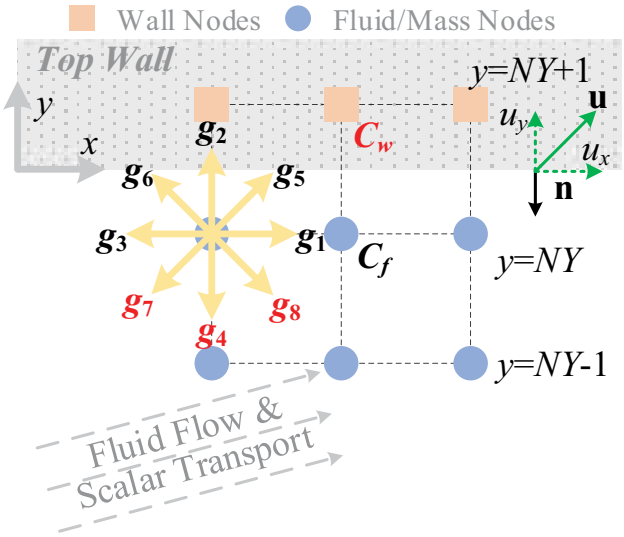

Fig. A1. Illustration of a top boundary.

In Eq. (A1), $c = \delta y/\delta t$ is the lattice speed contained in the discrete velocity $\mathbf{e}_i$. There are no available distribution functions streaming from wall nodes (y = NY + 1) to the boundary nodes (y = NY), thus g_4, g_7, g_8 are unknown distribution functions after the streaming operation. These unknown distribution functions should be prescribed and constrained by certain boundary conditions. For all interior nodes in the simulation domain, post-streaming distribution functions will be calculated based on neighboring post-collision distribution functions. Similarly, unknown post-streaming distribution functions of g_4, g_7 and g_8 on boundary nodes can also be calculated by post-collision distribution functions g_2^+, g_5^+, and g_6^+. Referring to Fig. A1, calculated post-streaming distribution functions g_2, g_5 and g_6 at boundary wall nodes (y = NY + 1) equal post-collision distributions g_2^+, g_5^+ and g_6^+ at boundary mass nodes (y = NY), respectively, as expressed in Eq. (A2).

$$\begin{cases} g_2\left(x,\mathrm{NY}+1\right)=g_2^+\left(x,\mathrm{NY}\right) \\ g_5\left(x+1,\mathrm{NY}+1\right)=g_5^+\left(x,\mathrm{NY}\right) \\ g_6\left(x-1,\mathrm{NY}+1\right)=g_6^+\left(x,\mathrm{NY}\right) \end{cases} \tag{A2}$$

From the approximation equation shown in Eq. (15), concentration gradients can be estimated by distribution functions at boundary wall nodes and boundary mass nodes, as shown in Eq. (A3).

$$\begin{cases} \dfrac{g_2\left(x,\mathrm{NY}+1\right)-g_2\left(x,\mathrm{NY}\right)}{\delta y}=w_2\dfrac{C_w-C_f}{\delta y} \\ \dfrac{g_5\left(x+1,\mathrm{NY}+1\right)-g_5\left(x,\mathrm{NY}\right)}{\delta y}=w_5\dfrac{\left(C_w+\dfrac{\delta C_w}{\delta x}\delta x\right)-C_f}{\delta y} \\ \dfrac{g_6\left(x-1,\mathrm{NY}+1\right)-g_6\left(x,\mathrm{NY}\right)}{\delta y}=w_6\dfrac{\left(C_w-\dfrac{\delta C_w}{\delta x}\delta x\right)-C_f}{\delta y} \end{cases} \tag{A3}$$

Note that in Eq. (A3), the variation of the wall concentration at a given node along the x direction is linearized using the first order Taylor expansion around the given node. Combining Eqs. (A2) and (A3) yields the relation between unknown post-streaming distribution functions and known post-collision distribution functions at boundary mass nodes, as shown in Eq. (A4).

$$\begin{aligned}\left(g_2+g_5+g_6\right)&=\left(g_2^+ +g_5^+ +g_6^+\right)-\frac{1}{6}\frac{\partial y\left(C_w-C_f\right)}{\delta y}\\&=\left(g_2^+ +g_5^+ +g_6^+\right)-\frac{1}{6}\delta y\frac{\partial C}{\partial y}\end{aligned}\tag{A4}$$

In Eq. (A4), weight coefficients in the lattice Boltzmann model are substituted, as $w_2 = 1/9$, $w_5 = 1/36$, $w_6 = 1/36$, and $w_2 + w_5 + w_6 = 1/6$. Also, the first-order normal derivative $\partial C/\partial \mathbf{n}$ on the right-hand side of Eq. (A4) is the replacement of the finite difference scheme approximation $(C_w - C_f)/\delta y$ on the right-hand side of Eq. (A3). Finally, Eq. (A5) can be derived when substitute $(g_2 + g_5 + g_6)$ from Eq. (A4) into Eq. (A1).

$$\frac{\delta y}{\delta t}\left(g_4+g_7+g_8\right)-\frac{\delta y}{\delta t}\left(g_2^+ +g_5^+ +g_6^+\right)=-\left(u_y C-\frac{\left(\tau-\frac{1}{2}\right)}{3}\frac{\left(\delta y\right)^2}{\delta t}\frac{\partial C}{\partial y}\right)\tag{A5}$$

The right-hand side of Eq. (A5) is actually total mass flux flowing from the top wall to the fluid phase (the surface normal $\mathbf{n}$ direction), and the coefficient term of the concentration gradient is the diffusion coefficient, that is, $D = (\tau_s - 1/2)(\delta h)^2/(3\delta t)$ from Eq. (8). Eq. (A5) is the general implementation form appearing in the mass flux boundary scheme for a top straight boundary. During the implementation process, unknown post-streaming distribution functions g_4, g_7 and g_8 can be calculated by the post-collision form of known distribution functions g_2^+, g_5^+ and g_6^+. The implementation form of Eq. (A5) can be expressed in a general form shown in Eq. (A6) or Eq. (14).

$$\begin{aligned}&\underbrace{\sum\nolimits_{\mathbf{e}_i\cdot\mathbf{n}>0} g_i\mathbf{e}_i\cdot\mathbf{n}}_{\text{unknown}}+\underbrace{\sum\nolimits_{\mathbf{e}_i\cdot\mathbf{n}\le 0} g_i^+\mathbf{e}_i\cdot\mathbf{n}}_{\text{known}}=\left(\mathbf{u}C-D\nabla C\right)\cdot\mathbf{n}=\mathbf{J}_\sigma\cdot\mathbf{n}\\&=\left[\left(u_x-\frac{D\partial C}{\partial x}\right)\mathbf{i}+\left(u_y-\frac{D\partial C}{\partial y}\right)\mathbf{j}+\left(u_z-\frac{D\partial C}{\partial z}\right)\mathbf{k}\right]\cdot\mathbf{n}\end{aligned}\tag{A6}$$

Although Eq. (A6) is the general form of Eq. (A5) which is valid for top boundaries, as will be discussed, Eq. (A6) is also correct for the bottom boundary. The top and the bottom boundaries are also representatives to the right and left boundaries due to the similarity of surface normal directions. Consequently, Eq. (A6) is valid for curved boundaries with staircase approximations comprising all straight boundaries. For the bottom boundary illustrated in Fig. A2, substituting concentration distribution functions (in post-streaming form) on the bottom boundary illustrated in Fig. A2 into Eq. (13) yields Eq. (A7).

$$\frac{\delta y}{\delta t}\underbrace{\left(g_2+g_5+g_6\right)}_{\text{unknown}}-\frac{\delta y}{\delta t}\underbrace{\left(g_4+g_7+g_8\right)}_{\text{known}}=u_y C-\frac{\tau}{3}\frac{\delta y^2}{\delta t}\frac{\partial C}{\partial y}\tag{A7}$$

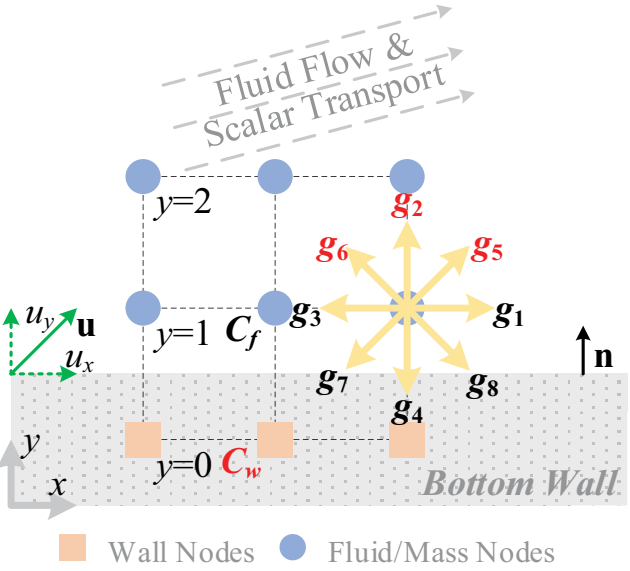

Fig. A2. Illustration of a bottom boundary.

Similar to Eq. (A2) and referring Fig. A2, calculated post-streaming distribution functions g_4, g_7 and g_8 at boundary wall nodes ($y = 0$) equal post-collision distributions g_4^+, g_7^+ and g_8^+ at boundary mass nodes ($y = 1$), respectively, as expressed in Eq. (A8).

$$\begin{cases}g_4\left(x,0\right)=g_4^+\left(x,1\right)\\g_7\left(x+1,0\right)=g_7^+\left(x,1\right)\\g_8\left(x-1,0\right)=g_8^+\left(x,1\right)\end{cases}\tag{A8}$$

From the approximation equations in Eq. (15), concentration gradients can be estimated by distribution functions at boundary wall nodes and boundary mass nodes, as shown in Eq. (A9).

$$\begin{cases}\dfrac{g_4\left(x,0\right)-g_4\left(x,1\right)}{\delta y}=w_4\dfrac{C_w-C_f}{\delta y}\\[2ex]\dfrac{g_7\left(x+1,0\right)-g_7\left(x,1\right)}{\delta y}=w_7\dfrac{\left(C_w+\dfrac{\delta C_w}{\delta x}\delta x\right)-C_f}{\delta y}\\[2ex]\dfrac{g_8\left(x-1,0\right)-g_8\left(x,1\right)}{\delta y}=w_8\dfrac{\left(C_w-\dfrac{\delta C_w}{\delta x}\delta x\right)-C_f}{\delta y}\end{cases}\tag{A9}$$

Combining of Eqs. (A8) and (A9) yields the relation between unknown post-streaming distribution functions and known post-collision distribution functions at boundary mass nodes, as shown in Eq. (A10).

$$\begin{aligned}\left(g_4+g_7+g_8\right)&=\left(g_4^+ +g_7^+ +g_8^+\right)-\frac{1}{6}\frac{\delta y\left(C_w-C_f\right)}{\delta y}\\&=\left(g_4^+ +g_7^+ +g_8^+\right)+\frac{1}{6}\delta y\frac{\partial C}{\partial y}\end{aligned}\tag{A10}$$

Finally, Eq. (A11) can be derived when substitute $(g_4 + g_7 + g_8)$ from Eq. (A10) into Eq. (A7).

$$\frac{\delta y}{\delta t}\left(g_2 + g_5 + g_6\right) - \frac{\delta y}{\delta t}\left(g_4^+ + g_7^+ + g_8^+\right) = u_y C - \frac{\left(\tau - \frac{1}{2}\right)}{3}\frac{\left(\delta y\right)^2}{\delta t}\frac{\partial C}{\partial y} \quad \text{(A11)}$$

So, it is demonstrated that Eq. (A11) can also described by the general form of Eq. (A6). For a standard square lattice, the non-dimensional lattice spacing $\delta h = \delta x = \delta y = 1$. The lattice time step δt is set to 1 so that the particles travel one lattice spacing during one time-step. So, in Eq. (A6), both $\mathbf{e}_i$ and $\mathbf{n}$ are unit vectors. The mass flux vector $\mathbf{J}_\sigma$ in Eq. (A6) is defined in the Cartesian coordinate system. The surface normal vector $\mathbf{n}$ pointing outward to the fluid phase works to redirect total mass flux to the normal vector direction (mass flux flows out of the solid phase toward the fluid phase, normal to the boundary). Also, the unit normal vector $\mathbf{n}$ should be in one of the three Cartesian coordinate directions. Thus, the present boundary scheme works for curved boundaries in staircase form. Finally, the relation between the first-order moment of distribution functions and heat/mass flux shown in Eq. (A6) is valid for both interior nodes and boundary nodes of the simulation domain.

Appendix B. Units conversion procedures

This appendix covers the conversion procedures between physical SI units and dimensionless LBM units. In the lattice Boltzmann method, units of physical quantities are usually dimensionless. Also, lattice spacing and time step are usually selected to be unity ($\delta x = \delta y = \delta t = 1$), thus the lattice speed $c = 1$. Furthermore, some special dimensionless numbers are frequently used to characterize the target system. For example, flows with same Reynolds numbers ($\mathrm{Re} = uL/\nu$) are equivalent for hydrodynamics, and solutions with same Schmidt numbers ($\mathrm{Sc} = \nu/D$) are equivalent for mass transport. A physical quantity Q can be written with a number and a unit, as shown in Eq. (A12).

$$Q = \bar{Q} \times C_Q \quad \text{(A12)}$$

in which Q is a physical quantity with a physical unit $[Q]$; $\bar{Q}$ is a dimensionless quantity with a dimensionless unit $[\bar{Q}] = 1$; C_Q is the conversion factor from $\bar{Q}$ to Q with a unit $[C_Q] = [Q]$.

Dimensionless numbers such as the Reynolds number and the Schmidt number should be invariant whether in a physical unit or in a dimensionless LBM unit. Assuming that flows with the same Re and Sc are equivalent, thus the conversion factors should be 1, as shown in Eq. (A13).

$$\mathrm{Re} = \overline{\mathrm{Re}} \Leftrightarrow C_{\mathrm{Re}} \doteq 1 \quad \text{(A13)}$$

There are a variety of conversion methods between physical SI units and dimensionless LBM units. The following procedures are followed in this paper. Note that a symbol with an overhead bar denotes a dimensionless quantity.

(1) General input parameters
Channel height: $H = 1 \times 10^{-3}$ m;
Kinematic viscosity of water: $\nu = 1.00 \times 10^{-6}$ m^2/s;
Density of water: $\rho = 1 \times 10^3$ kg/m^3;
Diffusion coefficient of ions in seawater: $D = 1.5 \times 10^{-9}$ m^2/s;

(2) Mesh resolution or node number of the channel height $H_{\mathrm{LBM}} = 100$;
Conversion factor of length: $C_H = H/H_{\mathrm{LBM}}$ (m);

(3) LBM density is generally selected to be 1: $\rho_{\mathrm{LBM}} = 1$;
Conversion factor of density: $C_\rho = \rho/\rho_{\mathrm{LBM}}$, (kg/m^3);

(4) Set the relaxation time for concentration field: $\tau_s = 0.51$;

(5) Set a reference diffusion coefficient $D_{\mathrm{ref}} = kD$ ($k > 0$, the coefficient k is case dependent);

For convenience, choose a unit lattice spacing and a unit time step: $\overline{\Delta x} = 1$; $\overline{\Delta t} = 1 \Rightarrow c = \overline{\Delta x}/\overline{\Delta t} = 1$.

(6) Schmidt number: $\mathrm{Sc} = \nu/D_{\mathrm{ref}}$;

(7) Conversion factor of time:

$$C_T = \frac{C_H^2\left(\tau_s - \frac{1}{2}\right)}{3D_{\mathrm{ref}}} \quad \text{(A14)}$$

(8) Conversion factor of velocity: $C_U = C_H/C_T$;

(9) Conversion factor of force per volume: $C_F = C_\rho C_H/C_T^2$;

(10) Diffusion coefficient in dimensionless unit:

$$\bar{D} = \frac{D_{\mathrm{ref}} C_T}{C_H^2} \quad \text{(A15)}$$

(11) Kinematic viscosity in dimensionless unit:

$$\bar{\nu} = \overline{D} \times \mathrm{Sc} \quad \text{(A16)}$$

(12) Relaxation time for fluid:

$$\tau = 3\bar{\nu} + \frac{1}{2} \quad \text{(A17)}$$

Usually, the calculated Mach number in the LBM unit system is larger than calculated in the physical unit system due to the smaller sound speed in LBM, otherwise the simulations would be too expensive. LBM simulates incompressible flow under a low Mach number condition ($\mathrm{Ma} = u/c_s < 0.3$, where u is the macroscopic flow velocity and c_s is the speed of sound) with a weak variation in density.